A reduced model for exact coherent states in high Reynolds number shear flows

Cédric Beaume

April 16, 2013

Abstract

We consider a shear flow driven in the streamwise direction by a sinusoidal body force varying in the wall normal direction and apply a lower branch scaling found by Wang *et al.* (2007) to reduce the dynamics to a set of two-dimensional PDEs valid at high Reynolds numbers. We then propose an iterative strategy to converge to lower branch exact coherent structures. This strategy only necessitates a two-dimensional projection of the streamwise velocity as initial condition and has been used to approach a stationary lower branch solution. Further strategies to find lower branch solutions are also proposed.

1 Introduction

Incompressible channel flow driven by in-plane boundary motion, referred to as plane Couette flow (figure 1), is a canonical model of a wall-bounded shear flow that is frequently used to investigate transition to turbulence. Although this flow is known to be linearly stable for all Reynolds numbers $Re = UL/\nu$, where U is the speed of the upper (or oppositely-moving lower) boundary, L is the half-channel width and ν is the kinematic viscosity [13], experiments and numerical simulations show a transition to a disordered flow state when Re exceeds a few hundred [11] (see figure 2). Theoretical progress on this transition process has been made by computing numerically exact coherent states (ECS): stationary or time-periodic solutions corresponding to fixed points in a (reduced) phase space [12, 7, 19, 4]. Analysis of a low-order model [20] and more systematic numerical studies [21, 14] reveal that these solutions seem to exist in an open interval of Reynolds number and are created through a saddle-node bifurcation. As the lower part of the branch produced by the saddle-node is not connected to the laminar solution, the mechanism underlying the existence of ECS is nonlinear. It consists in a cycle in which streamwise-invariant rolls (also called vortices) redistribute streamwise momentum by advection that leads to the creation of spanwise inhomogeneities, namely the streaks. The streaks then create wave-like structures varying in the streamwise direction that, in turn, feed the rolls to close the feedback loop. This cyclic mechanism, first articulated by Waleffe [20] is called the self-sustaining process and is illustrated in figure 3.

As the laminar profile is linearly stable at all Reynolds numbers, a finite-amplitude perturbation is necessary to trigger observable solutions such as turbulence (*cf.* diagram in figure 2). Given an appropriate spatial form for the perturbation, if the amplitude is

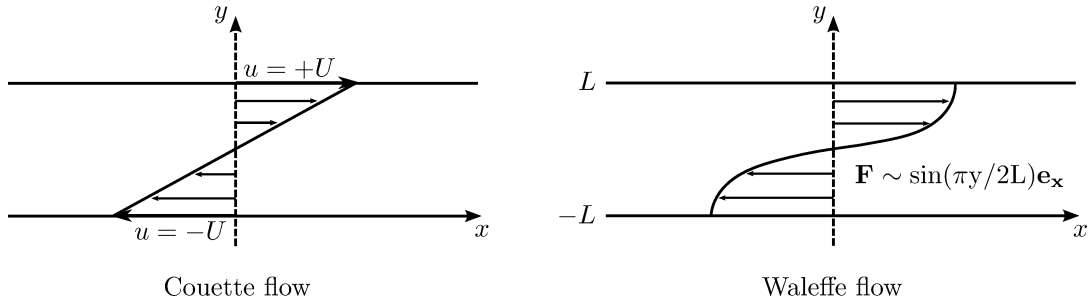Couette flow   Waleffe flow

Figure 1: Sketch of plane Couette and Waleffe flows. Plane Couette flow is driven by wall motion in the x direction, the top and bottom walls moving with opposite velocities $\pm U$. Plane Waleffe flow is driven by a volume force in the x direction. The forcing is half a sine period in the y coordinate. Note that the laminar flow is stable despite the presence of an inflection point owing to the proximity of free-slip walls.
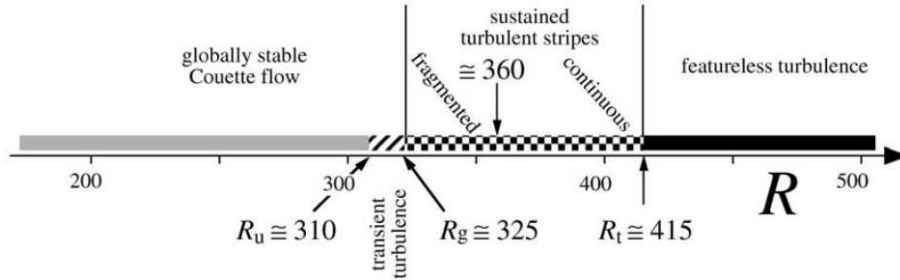

Figure 2: Behavior observed in experimental Couette flow. Once the Reynolds number (here R) is above 310, the system exhibits nonlinear dynamics. After Manneville [11].
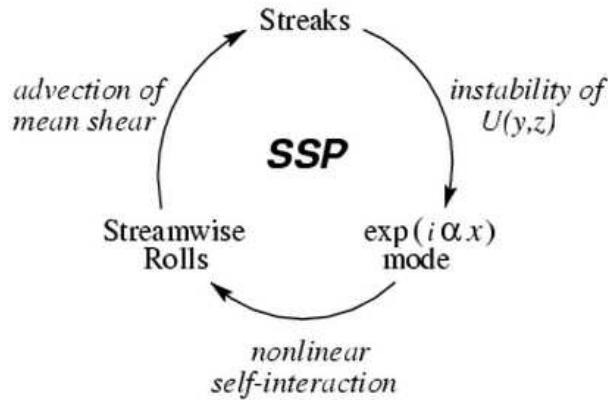

Figure 3: Self-sustaining process (SSP) sketched as a loop. After Waleffe [20].

2

too small, it decays. Conversely, if it is too large, the perturbation grows and a nonlinear behavior is reached. This defines a boundary between decay and growth that is called "the edge" and is populated by unstable nonlinear solutions. By studying the edge in small domains of different sizes, Schneider *et al.* [14] have obtained a family of ECS. They continued these solutions in Re to locate the saddle-nodes characteristic of these solutions and studied their stability, revealing that one of the lower branch solutions is only once unstable. It follows that lower branch ECS are likely to control some of the edge dynamics.

Wang *et al.* [21] established that lower branch solutions have an asymptotic structure as $Re \to \infty$ consisting of $\mathcal{O}(1)$ streaks and $\mathcal{O}(Re^{-1})$ rolls. They also identified that the fundamental streamwise-varying mode scales roughly as $\mathcal{O}(Re^{-1})$ and that higher harmonics are $o(Re^{-1})$. In the present study, we exploit these scalings to systematically derive a multiscale PDE model for plane parallel shear flow. The proposed reduced model appears to be conceptually simpler than a related asymptotic reduction of the Navier–Stokes equations by Hall & Sherwin [6]. Although both approaches enable the dynamics to be reduced from a 3D problem to two coupled 2D systems, the reduced formulation described here appears more straightforward. Moreover, this reduced model may be useful not only for studying large Reynolds number states, but also solutions in spatially-extended domains.

The following section introduces the new reduced model. After reviewing the asymptotic scaling observed by Wang *et al.* [21], the model is derived and interpreted. Section 3 deals with strategies for obtaining a nontrivial solution of the reduced model. In section 4, we explore the long-wavelength limit and present further reductions in this case. The last section briefly summarizes the work done and outlines work in progress.

2 Reduced model

2.1 Asymptotic law

Among the very few successful attempts to continue nonlinear solutions to relatively high Reynolds numbers (above 10^3) in plane Couette flow is a study by Wang, Gibson and Waleffe [21]. In their paper, the authors reported a computation in a box of size $2\pi \times 2 \times \pi$ where they decomposed the stationary lower branch solutions in Fourier modes in the streamwise direction,

$$\mathbf{u}(x, y, z) = \sum_{n=0}^{N} \mathbf{u_n}(y, z) \, e^{in\alpha x} + c.c., \tag{1}$$

where $\mathbf{u_n}$ represents the n-th Fourier mode, N is the order of truncation in the expansion, α is the fundamental wavenumber in the streamwise direction and *c.c.* denotes the complex conjugate.

The result of the numerical continuation of the stationary nonlinear solution is shown in figure 4. The solution is represented by its dominant components and their amplitude is plotted as a function of the Reynolds number. The figure indicates that the amplitudes scale like powers of the Reynolds number with the higher harmonics decaying faster than the lower ones. The stationary solution of interest is represented in figure 5. It consists of streaks u_0 and streamwise rolls (v_0, w_0) representing the average behavior in the streamwise direction. In addition to these quantities, a contribution $\mathbf{u_1}$ that fluctuates in the streamwise direction
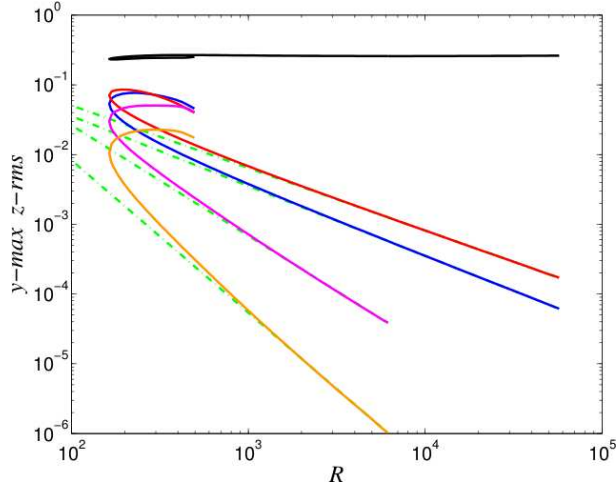
3

Figure 4: Results of the continuation in Reynolds number R of the stationary nonlaminar solution shown as the y-maximum of the z-root-mean-square of the leading Fourier modes. From top to bottom: the $\mathcal{O}(1)$ $n = 0$ mode u_0 (black), the $\mathcal{O}(R^{-0.9})$ fundamental mode $\mathbf{u_1}$ (red), the $\mathcal{O}(R^{-1})$ streamwise rolls (v_0, w_0) (blue), the $\mathcal{O}(R^{-1.6})$ second harmonics $\mathbf{u_2}$ (purple) and the $\mathcal{O}(R^{-2.2})$ third harmonics $\mathbf{u_3}$ (amber). After Wang *et al.* [21].
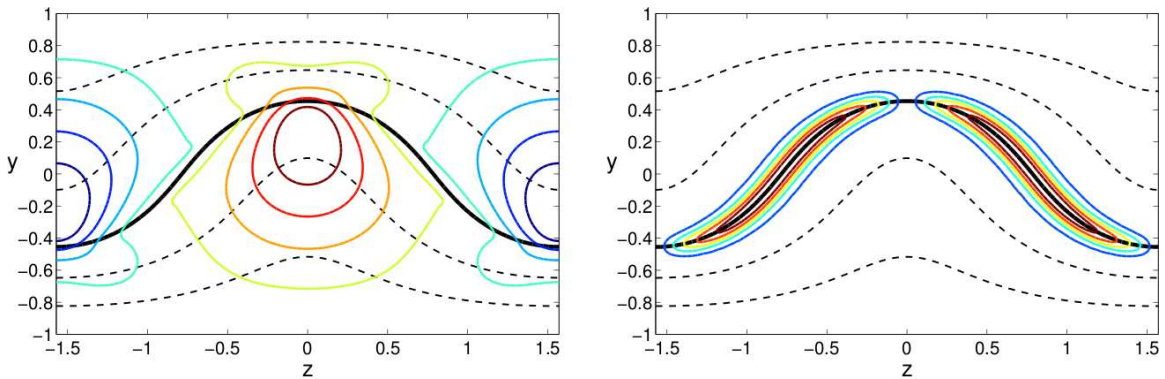

Figure 5: Representation of the solution studied by Wang *et al.* at $Re = 50171$. In both panels, the (black) open lines denotes contours of u_0, the thick line being $u_0 = 0$. The left (right) panel represents the contours of v_0 (v_1). After Wang *et al.* [21].

4

is present and accumulates around $u_0 = 0$. This specifies the location of the critical layer, a strong gradient zone centered on the isosurface on which the phase speed (here 0 since the solution is stationary) matches the streamwise flow velocity. Figure 4 shows that the streaks are $\mathcal{O}(1)$ at all Reynolds numbers and that the rolls and the fundamental mode scale roughly like the inverse of the Reynolds number. Note that beyond $Re = 6168$, the second and higher harmonics have been dropped but the computation continues to be well resolved, indicating that the $n = 0$ and fundamental modes suffice to approximate the solution when the Reynolds number is large.

Consequently, the streamwise structure of this type of nonlinear solution in plane Couette flow becomes simpler and simpler when the Reynolds number is increased. However, due to gradient sharpening in the vicinity of the critical layer, the solution structure becomes more and more difficult to resolve in the y–z plane. It is therefore possible to take advantage of this emergent $1/Re$ scaling by truncating the streamwise representation of the solution to the constant and fundamental modes to derive a reduced model for lower branch ECS at high Reynolds number.

2.2 Model derivation

In this work, we do not consider plane Couette flow, but a simpler case introduced by Waleffe [20] in which the flow is driven by a streamwise body force varying sinusoidally in the wall-normal direction with free-slip boundary conditions. A sketch of this flow is also shown in figure 1. The corresponding dimensionless Navier–Stokes equation for incompressible flow is

$$\partial_t \mathbf{u} + (\mathbf{u} \cdot \nabla) \mathbf{u} = -\nabla p + \tfrac{1}{Re} \nabla^2 \mathbf{u} + \tfrac{\sqrt{2}\pi^2}{4Re} \sin(\pi y/2), \tag{2}$$

$$\nabla \cdot \mathbf{u} = 0, \tag{3}$$

where t is the time variable, $\mathbf{u} = (u, v, w)$ is the 3D velocity field with components u, v and w in the x, y and z Cartesian directions respectively, p is the pressure and $Re = UL/\nu$ is the Reynolds number where U is the root-mean-square velocity of the laminar solution ($u = \sqrt{2}\sin(\pi y/2)$, $v = w = 0$ in dimensionless form), L is half the distance between the walls and ν is the kinematic viscosity of the fluid. These equations are complemented by stress-free boundary conditions along each wall:

$$\partial_y u(y = \pm 1) = v(y = \pm 1) = \partial_y w(y = \pm 1) = 0, \tag{4}$$

as well as periodic boundary conditions in the spanwise and streamwise directions. Although inflectional, the laminar flow is stable at all Re because of wall-blocking [20]. In the following, we refer to this flow as Waleffe flow. Its advantage, compared to plane Couette flow, lies in the use of the stress-free boundary-conditions, preventing the formation of diffusive boundary layers and facilitating Fourier-type expansions in all three coordinates.

To exploit the scaling behavior discussed in section 2.1, we first introduce a reduced Reynolds number $R = \epsilon Re = \mathcal{O}(1)$. Given the small parameter ϵ, we proceed to the following asymptotic expansion:

$$u = u_0 + \epsilon u_1 + \mathcal{O}(\epsilon^2), \tag{5}$$

$$v = \epsilon v_1 + \epsilon^2 v_2 + \mathcal{O}(\epsilon^3), \tag{6}$$

$$w = \epsilon w_1 + \epsilon^2 w_2 + \mathcal{O}(\epsilon^3), \tag{7}$$

5

where the subscript denotes the order in the ϵ-expansion. In this new framework, the streaks are contained in the variable u_0 and the rolls *as well as* the fundamental mode in the variables u_1, v_1, w_1 as they arise at first order (for notational simplicity, the subscript has a different meaning than in the previous section and in Wang *et al.* [21]). We also introduce a long spatial scale $X = \epsilon x$ to allow for modulation in the streamwise direction together with a slow time scale $T = \epsilon t$. The variables are treated by separating the fast-(x, t) average from the fluctuations:

$$f_n = \overline{f}_n(X, y, z, T) + f'_n(x, X, y, z, t, T), \tag{8}$$

where $\overline{f}_n$ stands for the (x, t) average of the field f_n and f'_n for its fluctuation. We then average the equations over x and t and examine the mean and fluctuation fields separately. The averaged equations read:

$$\partial_T \overline{u}_0 + \overline{u}_0 \partial_X \overline{u}_0 + \overline{v}_1 \partial_y \overline{u}_0 + \overline{w}_1 \partial_z \overline{u}_0 = \frac{1}{R} \nabla_\perp^2 \overline{u}_0 + \frac{\sqrt{2}\pi^2}{4R} \sin(\pi y/2), \tag{9}$$

$$\partial_T \overline{v}_1 + \overline{u}_0 \partial_X \overline{v}_1 + \overline{v}_1 \partial_y \overline{v}_1 + \overline{w}_1 \partial_z \overline{v}_1 +$$
$$\partial_y \left(\overline{v'_1 v'_1} \right) + \partial_z \left(\overline{w'_1 v'_1} \right) = -\partial_y \overline{p_2} + \frac{1}{R} \nabla_\perp^2 \overline{v}_1, \tag{10}$$

$$\partial_T \overline{w}_1 + \overline{u}_0 \partial_X \overline{w}_1 + \overline{v}_1 \partial_y \overline{w}_1 + \overline{w}_1 \partial_z \overline{w}_1 +$$
$$\partial_y \left(\overline{v'_1 w'_1} \right) + \partial_z \left(\overline{w'_1 w'_1} \right) = -\partial_z \overline{p_2} + \frac{1}{R} \nabla_\perp^2 \overline{w}_1, \tag{11}$$

$$\partial_X \overline{u}_0 + \partial_y \overline{v}_1 + \partial_z \overline{w}_1 = 0, \tag{12}$$

where $\nabla_\perp^2$ is the restriction of the Laplacian operator to the y–z plane. The fluctuation equations are:

$$\partial_t u'_1 + \overline{u}_0 \partial_x u'_1 + v'_1 \partial_y \overline{u}_0 + w'_1 \partial_z \overline{u}_0 = -\partial_x p'_1, \tag{13}$$

$$\partial_t v'_1 + \overline{u}_0 \partial_x v'_1 = -\partial_y p'_1, \tag{14}$$

$$\partial_t w'_1 + \overline{u}_0 \partial_x w'_1 = -\partial_z p'_1, \tag{15}$$

$$\partial_x u'_1 + \partial_y v'_1 + \partial_z w'_1 = 0. \tag{16}$$

Equations (9) and (12)–(16) are obtained at $\mathcal{O}(\epsilon)$ while equations (10) and (11) are obtained at $\mathcal{O}(\epsilon^2)$ (at $\mathcal{O}(\epsilon)$, $\overline{p}_1$ must satisfy a zero-gradient condition, hence the absence of pressure term in equation (9)). Note that at leading order ($\mathcal{O}(1)$), $u'_0 = p_0 = 0$. Moreover, fluctuating terms like $v'_1 v'_1 - \overline{v'_1 v'_1}$ enter at $\mathcal{O}(\epsilon^2)$ and therefore are not present in the fluctuation equations derived at $\mathcal{O}(\epsilon)$.

Further reduction can be achieved by exploiting the simple structure in the streamwise direction noted in section 2.1. The leading order streamwise velocity is $\mathcal{O}(1)$ and independent of the fast streamwise coordinate x. In addition, the first order wall-normal and spanwise velocities involve both the zero and fundamental modes. If we further assume that the leading order streamwise velocity and the fluctuations are independent of the slow

streamwise coordinate X, we can expand as follows:

$$\overline{u}_0 \sim \overline{u}_0^0(y, z, T), \tag{17}$$

$$\overline{v}_1 \sim \overline{v}_1^0(y, z, T) + \overline{v}_1^\delta(y, z, T)e^{i\delta X} + c.c., \tag{18}$$

$$\overline{w}_1 \sim \overline{w}_1^0(y, z, T) + \overline{w}_1^\delta(y, z, T)e^{i\delta X} + c.c., \tag{19}$$

$$u_1' \sim u_1'(y, z, t, T)e^{i\alpha x} + c.c., \tag{20}$$

$$v_1' \sim v_1'(y, z, t, T)e^{i\alpha x} + c.c., \tag{21}$$

$$w_1' \sim w_1'(y, z, t, T)e^{i\alpha x} + c.c., \tag{22}$$

where $\delta = \mathcal{O}(1)$ is the wavenumber in the long ($\mathcal{O}(\epsilon^{-1})$) streamwise scale, α is the wavenumber in the short ($\mathcal{O}(1)$) streamwise scale. The streamwise independent variables are noted with a 0 superscript, those varying on the long streamwise scale with a δ superscript and the fluctuations with a prime. As $\overline{u}_0 = \overline{u}_0^0(y, z, t, T) \neq f(X)$, the mean incompressibility condition (equation (12)) yields the following constraints:

$$\partial_y \overline{v}_1^0 + \partial_z \overline{w}_1^0 = 0, \tag{23}$$

$$\partial_y \overline{v}_1^\delta + \partial_z \overline{w}_1^\delta = 0. \tag{24}$$

This reduction enables us to introduce a streamfunction-vorticity formulation:

$$\overline{v}_1^0 = -\partial_z \overline{\psi}_1^0, \qquad \overline{w}_1^0 = \partial_y \overline{\psi}_1^0, \qquad \overline{\omega}_1^0 = \nabla_\perp^2 \overline{\psi}_1^0, \tag{25}$$

$$\overline{v}_1^\delta = -\partial_z \overline{\psi}_1^\delta, \qquad \overline{w}_1^\delta = \partial_y \overline{\psi}_1^\delta, \qquad \overline{\omega}_1^\delta = \nabla_\perp^2 \overline{\psi}_1^\delta. \tag{26}$$

Here, $\overline{\psi}_1^0$ ($\overline{\psi}_1^\delta$) stands for the streamfunction for the velocities with a 0 (δ) superscript and $\overline{\omega}_1^0$ ($\overline{\omega}_1^\delta$) is the associated vorticity in the y–z plane. Given these further simplifications, the system (9)–(16) can be rewritten:

$$\partial_T \overline{u}^0 + \partial_y \overline{\psi}_1^0 \partial_z \overline{u}^0 - \partial_z \overline{\psi}_1^0 \partial_y \overline{u}^0 = \frac{1}{R}\nabla_\perp^2 \overline{u}^0 + \frac{\sqrt{2}\pi^2}{4R}\sin(\pi y/2), \tag{27}$$

$$\partial_T \overline{\omega}_1^0 + J\left(\overline{\psi}_1^0, \overline{\omega}_1^0\right) + 2\mathcal{R}\left[J\left(\overline{\psi}_1^{\delta*}, \overline{\omega}_1^\delta\right)\right] +$$
$$2\left(\partial_y^2 - \partial_z^2\right)\overline{\mathcal{R}(v_1'w_1'^*)} + 2\partial_z\partial_y\left(\overline{w_1'w_1'^*} - \overline{v_1'v_1'^*}\right) = \frac{1}{R}\nabla_\perp^2\overline{\omega}_1^0, \tag{28}$$

$$\partial_T \overline{\omega}_1^\delta + i\delta\left[\overline{u}^0\overline{\omega}_1^\delta + \partial_y\overline{u}^0\partial_y\overline{\psi}_1^\delta + \partial_z\overline{u}^0\partial_z\overline{\psi}_1^\delta\right] +$$
$$J\left(\overline{\psi}_1^0, \overline{\omega}_1^\delta\right) + J\left(\overline{\psi}_1^\delta, \overline{\omega}_1^0\right) = \frac{1}{R}\nabla_\perp^2\overline{\omega}_1^\delta, \tag{29}$$

where $J(f, g) = \partial_y f \partial_z g - \partial_z f \partial_y g$ is the Jacobian of the functions f and g, $\mathcal{R}(f)$ is the real part of the function f and the superscript $*$ indicates the complex conjugate. These equations are to be solved together with the fluctuation equations:

$$\partial_t u_1' + i\alpha\overline{u}^0 u_1' + v_1'\partial_y\overline{u}^0 + w_1'\partial_z\overline{u}^0 = -i\alpha p_1' + \frac{\epsilon}{R}\nabla_\perp^2 u_1', \tag{30}$$

$$\partial_t v_1' + i\alpha\overline{u}^0 v_1' = -\partial_y p_1' + \frac{\epsilon}{R}\nabla_\perp^2 v_1', \tag{31}$$

$$\partial_t w_1' + i\alpha\overline{u}^0 w_1' = -\partial_z p_1' + \frac{\epsilon}{R}\nabla_\perp^2 w_1', \tag{32}$$

$$i\alpha u_1' + \partial_y v_1' + \partial_z w_1' = 0, \tag{33}$$

where the streamfunctions are determined from equations (25) and (26). In writing the fluctuation system (30)–(33), the higher order diffusion term has been retained in order to regularize the equations, hence their occurrence with an ϵ prefactor.

2.3   Discussion

A classic picture of linearly stable shear flow dynamics is the presence of three unconnected families of solutions:

- the laminar solution: here, $\overline{u}^0 = \sqrt{2}\sin(\pi y/2)$ with the other variables vanishing

- turbulent trajectories: strongly nonlinear solutions with nontrivial time behavior

- intermediate states that include the lower branch states: stationary or periodic solutions in time corresponding to fixed points in a (reduced) phase space

The model derived in section 2.2 is intended to capture lower branch ECS as well as similar states exhibiting amplitude modulation in the streamwise direction. The use of an asymptotic expansion in our derivation can be interpreted as a zoom in a particular regime in which at least one lower branch solution is present. Only solutions in this scaling regime can be captured and we anticipate the reduced model to preclude turbulent states as well as some of the fixed points.

In the usual derivation of equations for mean quantities from the Navier–Stokes equations, one ends up with products of fluctuations, namely the Reynolds stresses. The primary challenge is then to find a closure for these Reynolds stresses [18]. In the present case, the use of multiscale analysis not only allows us to study streamwise modulation but also to obtain a natural closure using the time-dependent fluctuation equations (30)–(33).

The model (27)–(33) contains the essential ingredient for the existence of nontrivial solutions: the self-sustaining process [20]. For short to moderate streamwise domains ($\overline{\omega}_1^\delta = 0$), this process is as follows:

- streamwise rolls $\overline{\omega}_1^0$ redistribute the streamwise momentum $\overline{u}^0$ by advection to create spanwise inhomogeneities

- spatial inhomogeneities of $\overline{u}^0$ generate a wave-like instability in the streamwise direction by feeding the fluctuations (u_1', v_1', w_1')

- the fluctuations, through the Reynolds stresses in equation (28), reenergize the rolls $\overline{\omega}_1^0$

This cycle explains why solutions other than the base flow can persist in plane Waleffe flow and be captured in our model.

Finally note that the time separation between the mean variables evolving slowly as $T = \epsilon t$ and the fluctuations evolving on the rapid time scale t leads to the quasi-linearity of the fluctuation equations (30)–(33). Indeed, the pseudo-nonlinear terms in these equations always involve a product between one fluctuation and $\overline{u}^0$. While the former variable evolves rapidly, the latter evolves far more slowly, making $\overline{u}^0$ roughly a constant during time scales on which the fluctuations evolve. Although this quasi-linearity can enable analytical progress, it also causes the amplitude of the fluctuations to be indeterminate. This characteristic is common in models derived using multiscale analysis and has previously been observed in multiscale models for the tropics [10] as well as the description of the interaction on time disparate scales of ocean dynamics [5] and of atmospheric flows [8]. To deal with this pathology, one needs to adapt the technique, as described in the next section.
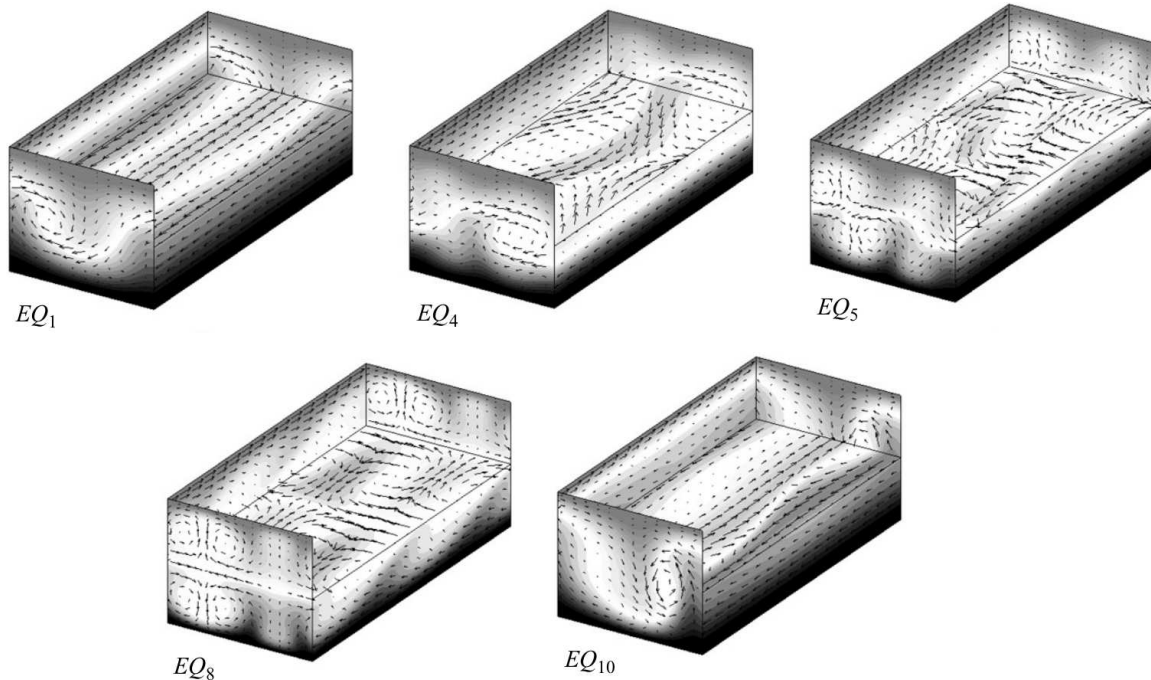
Figure 6: Equilibrium solutions of plane Couette flow in a $2\pi/1.14 \times 2 \times 2\pi/2.5$ domain at $Re = 400$. The greyscale indicates the streamwise velocity of the fluid: light (dark) grey shows fluid moving at $u = +1$ ($u = -1$). Arrows indicate in-plane velocity. The top half of the fluid is cut away to show the (u, w) velocity in the $y = 0$ midplane. Note that solution EQ_1 is a lower branch Nagata solution. After Gibson *et al.* [4].

3   Computing a lower branch exact coherent structure

We look for solutions of the same type as those computed by Gibson *et al.* [4] and shown in figure 6. As for most of those presented in the literature [21, 14, 3], these solutions have been computed in a small ($\mathcal{O}(1)$ aspect-ratio) domain. As a natural first step, we similarly restrict our search to solutions with no long-scale dynamics, for which $\overline{\psi}_1^\delta = 0$ ($\overline{\omega}_1^\delta = 0$).

By taking the divergence of the fluctuation equations (30)–(32) and applying the incompressibility condition (33), we find an equation for the pressure that does not involve u_1':

$$(\alpha^2 - \nabla_\perp^2)p_1' = 2i\alpha(v_1'\partial_y\overline{u}^0 + w_1'\partial_z\overline{u}^0). \tag{34}$$

Neither equation (34) nor equations (31) and (32) for v_1', w_1' involve u_1'. As this fluctuation field is not needed to compute the Reynolds stresses in equations (28) and (29), equation

(30) does not need to be solved. Hence, the "maximally simplified" reduced model is:

$$\epsilon \partial_t \overline{u}^0 + \partial_y \overline{\psi}_1^0 \partial_z \overline{u}^0 - \partial_z \overline{\psi}_1^0 \partial_y \overline{u}^0 = \frac{1}{R} \nabla_\perp^2 \overline{u}^0 + \frac{\sqrt{2}\pi^2}{4R} \sin(\pi y/2), \tag{35}$$

$$\epsilon \partial_t \overline{\omega}_1^0 + J\left(\overline{\psi}_1^0, \overline{\omega}_1^0\right) + 2\left(\partial_y^2 - \partial_z^2\right) \overline{\mathcal{R}(v_1' w_1'^*)} + 2\partial_z \partial_y \left(\overline{w_1' w_1'^*} - \overline{v_1' v_1'^*}\right) = \frac{1}{R} \nabla_\perp^2 \overline{\omega}_1^0, \tag{36}$$

$$(\alpha^2 - \nabla_\perp^2) p_1' = 2i\alpha(v_1' \partial_y \overline{u}^0 + w_1' \partial_z \overline{u}^0), \tag{37}$$

$$\partial_t v_1' + i\alpha \overline{u}^0 v_1' = -\partial_y p_1' + \frac{\epsilon}{R} \nabla_\perp^2 v_1', \tag{38}$$

$$\partial_t w_1' + i\alpha \overline{u}^0 w_1' = -\partial_z p_1' + \frac{\epsilon}{R} \nabla_\perp^2 w_1', \tag{39}$$

where we have replaced T by the non-asymptotic form t/ϵ to have a single time variable.

We proceed by choosing $Re = 400$ ($\epsilon = 1/400$ and $R = 1$), the streamwise wavenumber $\alpha = 0.5$, and the spanwise extent of the domain to be π. The domain is discretized using an equispaced mesh in both the wall-normal y and the spanwise z coordinates. We used 64 points in both directions which proved sufficient for convergence when compared with a 96-point mesh. The equations are treated in spectral space, using the Fast Fourier transform in the periodic direction z and the Fast Cosine Transform-I or Fast Sine Transform-I in the y direction, depending on the boundary conditions [2]. The nonlinear products are computed in physical space, and a classic 2/3 dealiasing rule is applied before each nonlinear computation to prevent frequency folding. Spatial derivatives are computed in spectral space. Derivatives in z are computed by a multiplication of the spectral coefficients by ik where k is the wavenumber corresponding to the spectral coefficient. Derivatives in y are treated similarly, bearing in mind that differentiating a field expanded in sine functions yields cosine coefficients and *vice versa*.

3.1 Iterative algorithm

The solutions we seek to compute are unstable and cannot be reached via time-integrating the reduced equations. As shown in figures 5 and 6, they also have a non-trivial spatial structure and the absence of a very precise initial condition prevents the successful use of a fixed point method. Finally, these solutions do not bifurcate from the laminar base state, so continuation from that state is not useful. Fortunately, we can exploit the mathematical structure of the simplified reduced model (35)–(39). The mean variables $\overline{u}^0$ and $\overline{\omega}_1^0$ and the fluctuations p_1', v_1' and w_1' evolve over different time scales. By separating the fast fluctuation system (37)–(39) from the slow averaged one, the former becomes linear as the mean quantities do not evolve over the fast time scale. The advantage of this decoupling is that, owing to the linearity of equations (37)–(39), the fluctuations can be thought of as solutions of an eigenvalue problem with a temporal growth rate λ. The crucial observation is that if an eigenvector has a vanishing real growth rate, it is a stationary solution of equations (37)–(39). Of course, the amplitude of the fluctuations is then indeterminate and must be formally introduced as a new scalar unknown A. For such fluctuations and given A, if the mean fields $\overline{u}^0$ and $\overline{\omega}_1^0$ are stationary, then we have a stationary solution.

To apply this decoupling algorithm we proceed as follows:

- Choose a fluctuation amplitude A

- While the growth rate λ is not converged:

- – Compute the fastest non-oscillatory growing (or most slowly decaying) fluctuation mode and its real growth rate λ using equations (37)–(39)

- – Compute the Reynolds stresses using A and the fluctuation fields so obtained

- – Time-advance $\overline{u}^0$ and $\overline{\omega}_1^0$ to steady state using equations (35) and (36)

- Store the converged λ and adjust A to drive λ to zero

Thus, given an initial condition for $\overline{u}^0$, this algorithm requires iteration on the amplitude A. We describe the method to obtain the initial condition for $\overline{u}^0$ below. Solution of the fluctuation eigenvalue problem is performed using an Arnoldi iteration [9]. This computation is equivalent to finding the stability of $\overline{u}^0$ with respect to perturbations varying sinusoidally in the streamwise direction. In this sense, one wants to focus on the least unstable, hence more realizable and dynamically influential solutions. This is achieved by picking the fastest growing (or most slowly decaying) mode. Moreover, we choose to isolate non-oscillatory modes ($\mathcal{I}(\lambda) = 0$) to compute stationary ECS. It should be possible to find a traveling-wave ECS by choosing an oscillatory mode ($\mathcal{I}(\lambda) \neq 0$). Finally, time integration of equations (35) and (36) is carried out using a semi-implicit third order Runge–Kutta scheme [17].

3.2 Results

3.2.1 Initial condition

We describe here how we obtained an initial condition for the algorithm described in the previous section. We remind the reader that we do not need a full initial condition as only $\overline{u}^0$ is required to initiate the calculation of the fluctuations. We generate a physically reasonable initial profile for $\overline{u}^0$ by imposing faux rolls $\overline{\psi}_1^0$ and then solving for $\overline{u}^0$ from (35) with $\overline{\psi}_1^0$ frozen. We choose a simple shape for the rolls: $\overline{\psi}_1^0(y, z) = \Psi \sin(2z) \cos(\pi y/2)$, with Ψ an arbitrary amplitude to be tuned to get the desired initial condition. Figure 7 depicts a family of initial conditions parametrized by Ψ. In this way, we have generated a whole family of initial conditions having the characteristic u-shape of the desired ECS. Given these results, we choose to use the profile obtained for $\Psi = -20$ (figure 7(b), top right).

3.2.2 Algorithm behavior

We executed the algorithm for different values of the fluctuation amplitude A and summarize the results of the iterations in figure 8. The convergence of the leading real eigenvalue λ_{max} is monitored which allows us to identify two different regimes. For small amplitudes (figure 8(a)), the algorithm converges but λ_{max} is not necessarily 0. Figure 9 shows $\overline{u}^0$ at convergence for $A = 5$ to $A = 6.8$. These converged iterations indicate that for small fluctuation amplitudes, the streamwise velocity $\overline{u}^0$ relaxes to reach a converged state that is close to the laminar state (figure 9(a)). When the amplitude is large enough, the algorithm converges to a $\overline{u}^0$ that now has a pronounced u-shape (figure 9(b) and (c)). By comparing converged iterates for $A = 6.6$ and $A = 6.8$, it is evident that the increase in the fluctuation amplitude leads to a stretching of the $\overline{u}^0 = 0$ line.
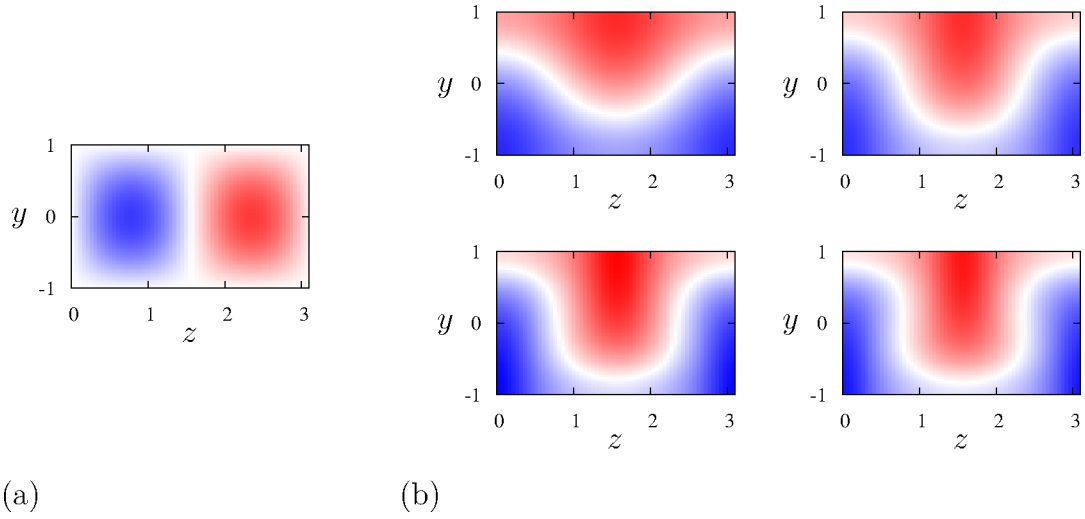
11

(a)   (b)

Figure 7: (a) Faux rolls $\overline{\psi}_1^0(y,z) = \Psi \sin(2z)\cos(\pi y/2)$ used to create the initial guess for $\overline{u}^0$ in (b). Different streak profiles are plotted in (b) corresponding to different values of Ψ, from $\Psi = -10$ (top left) to $\Psi = -40$ (bottom right) with an increment of -10. Red indicates positive velocity, blue indicated negative velocity and white $\overline{u}^0 = 0$. The initial condition used in the following is the solution plotted in the top right panel, corresponding to $\Psi = -20$.
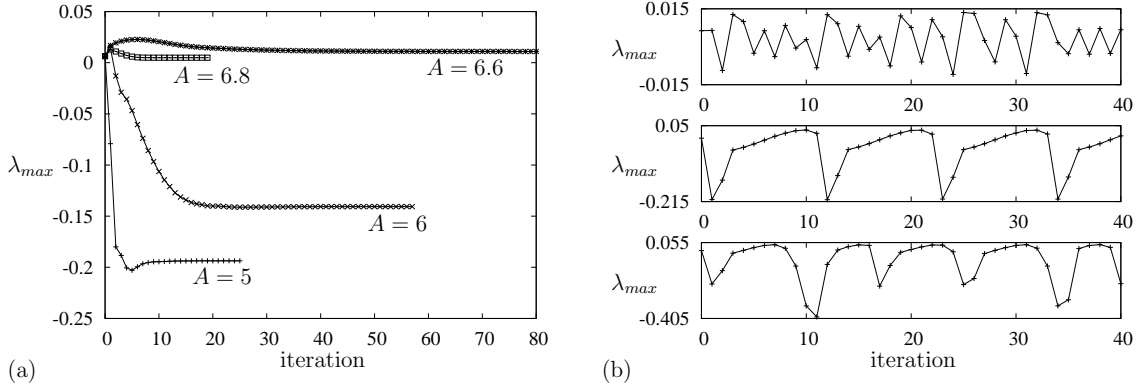

(a)   (b)

Figure 8: (a) Plot of the leading real eigenvalue λ_{max} as a function of the iteration number for different fluctuation amplitudes. The algorithm is stopped when λ_{max} is converged to the sixth digit: $\lambda_{max} = -0.19366$ for $A = 5$, $\lambda_{max} = -0.14064$ for $A = 6$, $\lambda_{max} = 0.01099$ for $A = 6.6$, $\lambda_{max} = 0.00489$ for $A = 6.8$. (b) From top to bottom, the leading real eigenvalue is shown as a function of iteration number for $A = 7$, $A = 7.5$ and $A = 8$.
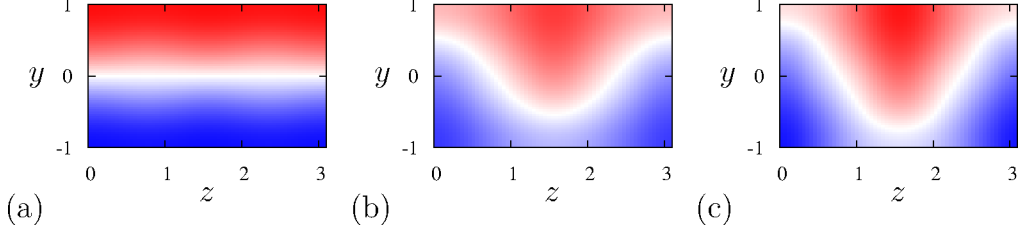
12

Figure 9: Converged iterations represented via $\overline{u}^0$ for (a) $A = 5$ (a similar solution is obtained for $A = 6$), (b) $A = 6.6$ and (c) $A = 6.8$. The color code is the same as in figure 7.
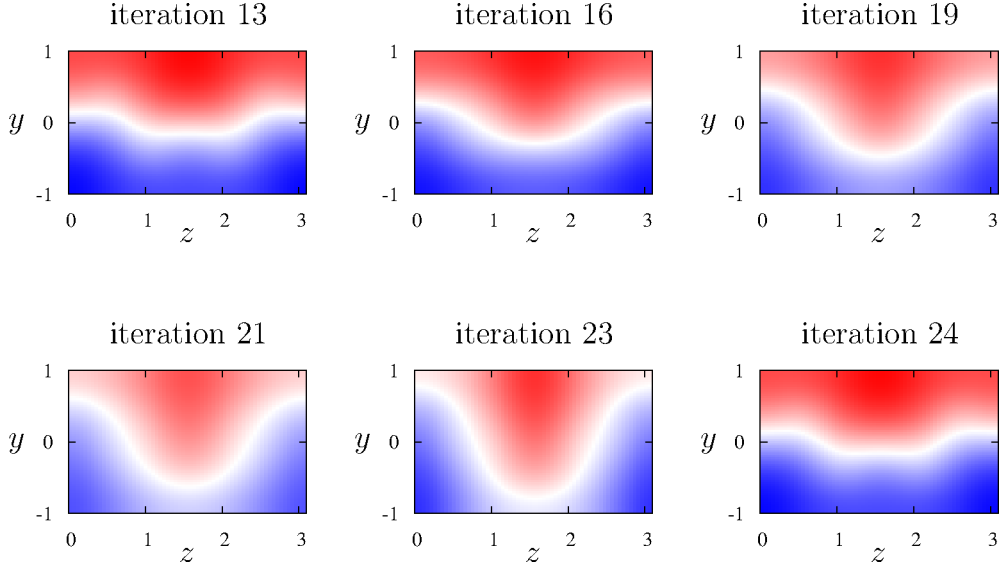

Figure 10: Streamwise mean velocity $\overline{u}^0$ during iterations 13, 16, 19, 21, 23 and 24 obtained with $A = 7.5$. A global view of the behavior of the algorithm for this value of the fluctuation amplitude is available in figure 8(b) center plot. The same color code is used as in figure 7.

If the amplitude of the fluctuations is increased approximately $A = 6.8$, another regime is reached. As illustrated in figure 8(b), the iterations do not converge but instead produce oscillations around $\lambda_{max} = 0$ with large excursions to negative values. The oscillations are bounded although the interval increases as A is increased with the upper bound increasing slowly while the lower bound decreases rapidly. Some iterates computed during the simulation run with $A = 7.5$ are shown in figure 10. These iterates are taken along the second "cycle" in figure 8(b) center plot. At iteration 13, $\overline{u}^0$ is close to the laminar profile, with the $\overline{u}^0 = 0$ isosurface rather flat. Then, until iteration 23, the streaks build progressively owing to the forcing generated by the fluctuations. The u-shape of the $\overline{u}^0 = 0$ surface becomes more and more pronounced until, at iteration 24, $\overline{u}^0$ becomes remarkably similar to that at iteration 13. This cycle is repeated, although with slight "phase" changes during further iterations.

Regarding the Reynolds stresses as a forcing term, we can interpret the amplitude of the fluctuations as the (square root of the) amplitude of the forcing. When A is too
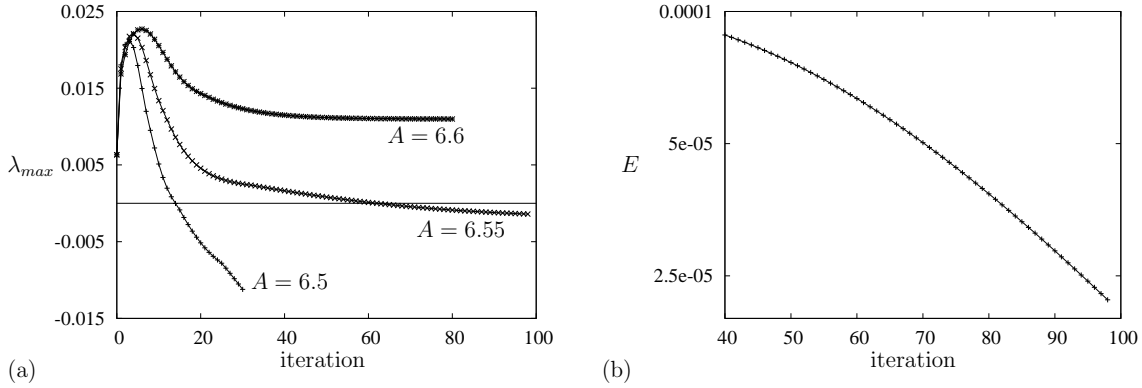
13

Figure 11: (a) Plot of the leading real eigenvalue λ_{max} as a function of the iteration for different amplitudes of the fluctuations. The horizontal line indicates $\lambda_{max} = 0$. Only the curve for $A = 6.6$ is stopped at convergence, that for $A = 6.5$ goes way below $\lambda_{max} = 0$ and that at $A = 6.55$ converges very slowly. (b) Evolution of the difference E between two successive iterates of λ_{max} for $A = 6.55$ on logarithmic scale.

small, the dynamics are diffusion dominated, with any initial condition relaxing to the laminar solution except for a slight perturbation that is maintained by fluctuations (that have fixed amplitude). This behavior is observed for $A \leq 6$. For sufficiently large A, the Reynolds stresses are strong enough to compete with diffusion in equation (36), and allow the fluctuations to maintain a nontrivial profile as seen for $A = 6.6$ and $A = 6.8$. Finally, if A is too large, the Reynolds stresses dominate diffusion and an oscillatory behavior sets in, as observed for $A \geq 7$ and exemplified at $A = 7.5$ in figure 10. At these large values of the fluctuation amplitude, the mean variables $\overline{u}^0$ and $\overline{\omega}_1^0$ over-respond to the fluctuations due to their exaggerated amplitude, and the solution oscillates around what may be the actual fixed point.

The results shown in figure 8(a) show that the converged λ_{max} first increases as A increases, eventually becoming positive. Then, at $A \approx 6.6$, λ_{max} starts decreasing before the oscillatory regime is reached. These results suggest that there is at least one value of the fluctuation amplitude A_{opt} for which $\lambda_{max} \rightarrow 0$. This amplitude lies in the range $6 < A < 6.6$ and will lead to a stationary solution of the problem (35)–(39), that is, a lower branch ECS. A second value $6.8 < A'_{opt} < 7$ may lead to a stationary solution: as A is increased above 6.6, λ_{max} decreases but is still positive for $A = 6.8$ before oscillating for $A \geq 7$. This solution, if captured by our reduced model, presumably would have the same structure and would be related to the lower branch solution found with A_{opt}.

3.2.3 Towards a solution

Given the results of the preceding section, we focus on the interval $6 < A < 6.6$. Figure 11 shows the results obtained from simulations with $A = 6.5$, $A = 6.55$ and $A = 6.6$. As in figure 8, the leading real eigenvalue converges to $\lambda_{max} = 0.01099$ for $A = 6.6$ after approximately 80 iterations. When $A = 6.5$, λ_{max} decreases quickly to converge to a negative value. This indicates that $6.5 < A_{opt} < 6.6$. A typical result for A within this interval is
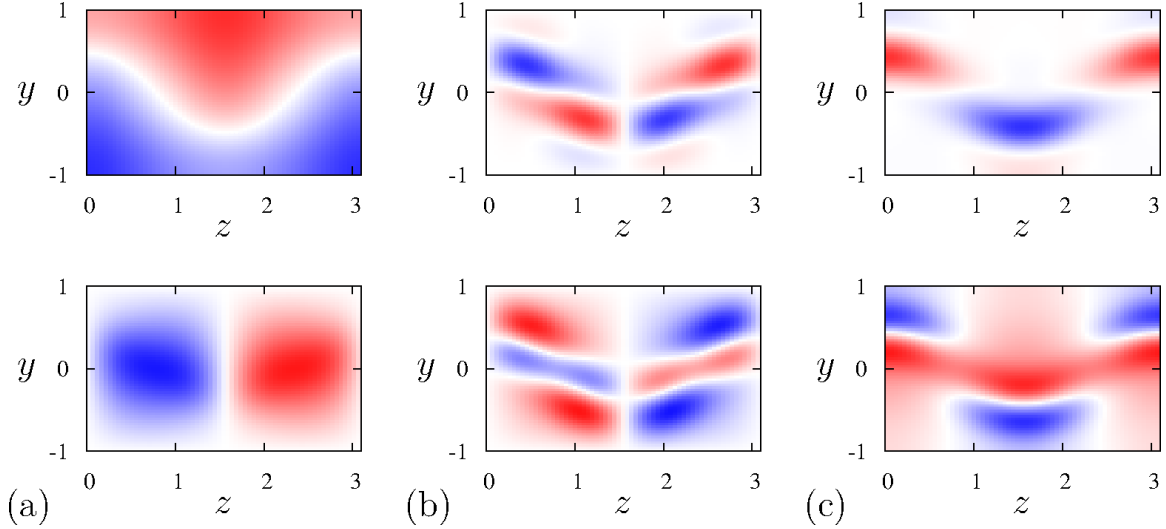
14

Figure 12: Flow fields at the last iteration for $A = 6.55$ (see figure 11). (a) Top: $\overline{u}^0$, bottom: $\overline{\psi}_1^0$. (b) Top: $\mathcal{R}(v_1')$, bottom: $\mathcal{I}(v_1')$. (c) Top: $\mathcal{R}(w_1')$, bottom: $\mathcal{I}(w_1')$. In all cases, blue (red) represents negative (positive) values of the field.

reported in figure 11. Even after nearly 100 iterations, λ_{max} is not fully converged. The difference E between two successive iterates is plotted as a function of the iteration number in figure 11(b). The error E decreases faster than exponentially, indicating convergence is likely. However, the slope is very small and a large number of iterations is therefore required to satisfy a reasonable convergence criterion.

The converged values of λ_{max} for different A indicate that the fluctuation amplitude of the actual lower branch solution is close to 6.55. Moreover, the solutions obtained by varying A are very similar (as the reader can convince himself by comparing figures 9(b) and (c)). This suggest the state shown in figure 12, obtained at the last iteration for $A = 6.55$, is very close to the actual lower branch solution. This state is comprised of streaks $\overline{u}^0$ and rolls $\overline{\psi}_1^0$, with the rolls differing from the initial condition (figure 7) by a slight tilt. The fluctuations are concentrated around $\overline{u}^0 = 0$, indicating the emergence of a critical layer. This state can be used as a very good initial guess in a Newton solver to converge to the desired precision to the lower branch solution, a task we leave for future work.

4   Long-wavelength limit

It is of interest to consider the long-wavelength limit of the lower branch ECS. Indeed, Hall & Sherwin [6] have shown that the minimum drag state for lower branch ECS occurs as the fundamental streamwise wavenumber α of the fluctuation fields tends to zero. Here, we show that a further reduction of our asymptotically reduced model of plane Waleffe flow can be obtained in the limit $Re \to \infty$ and $\alpha \to 0$ with $\hat{R} \equiv \alpha Re \gg 1$. In this limit, the single streamwise scale $\chi \equiv \alpha x$ replaces the fast x scale and the modulation scale $X \equiv \epsilon x$, where, again, $\epsilon = \mathcal{O}(1/Re)$ is indicative of the amplitude of both the roll and streamwise-varying

(*i.e.* fluctuation) components of the lower-branch ECS. Two time scales are required, with the fluctuation dynamics occurring on the scale $\tau \equiv \alpha t$ and the mean fields evolving more slowly, on the scale $T \equiv \epsilon t$. It should be emphasized at the outset that the distinguished limit in which $\alpha \to 0$ with $\alpha = \mathcal{O}(1/Re)$ requires a rather different analysis in which: (i) the fluctuation dynamics are, at leading order, modified by viscous effects across the entire domain, not just within thin boundary and critical layers; and (ii) the fluctuation dynamics are fully nonlinear rather than quasi-linear, resulting in the mixing of streamwise modes. This limit, although of interest, is not pursued here.

Again motivated by the results of Wang *et al.* [21], we expand the velocity fields as

$$u \quad \sim \quad \left(\overline{u}_0 + u_0'\right) + \epsilon\left(\overline{u}_1 + u_1'\right) + \dots, \tag{40}$$

$$v \quad \sim \quad \epsilon\left(\overline{v}_1 + v_1'\right) + \epsilon^2\left(\overline{v}_2 + v_2'\right) + \dots, \tag{41}$$

$$w \quad \sim \quad \epsilon\left(\overline{w}_1 + w_1'\right) + \epsilon^2\left(\overline{w}_2 + w_2'\right) + \dots, \tag{42}$$

where generic dependent variable $f(x, y, z, t) = \overline{f}(y, z, T) + f'(\chi, y, z, \tau, T)$; that is, an overbar refers to a χ and fast time τ average and a prime to a fluctuation about that mean. Substituting into equations (2) and (3) yields $u_0' = p_0 = p_1 = 0$ in the limit being considered. The resulting leading order mean equations can be expressed as

$$\partial_T \overline{u}_0 + J(\overline{\psi}_1, \overline{u}_0) \quad = \quad \frac{1}{R}\nabla_\perp^2 \overline{u}_0, \tag{43}$$

$$\partial_T \overline{\Omega}_1 + J(\overline{\psi}_1, \overline{\Omega}_1) \quad = \quad \left(\partial_z^2 - \partial_y^2\right)\overline{v_1' w_1'} + \partial_z\left[\partial_y\left(\overline{v_1' v_1'} - \overline{w_1' w_1'}\right)\right] + \frac{1}{R}\nabla_\perp^2 \overline{\Omega}_1, \tag{44}$$

$$\nabla_\perp^2 \overline{\psi}_1 \quad = \quad \overline{\Omega}_1, \tag{45}$$

where $\overline{\Omega}_1 = \partial_y \overline{w}_1 - \partial_z \overline{v}_1$ is the mean vorticity with $\overline{\psi}_1$ the associated streamfunction, $R \equiv \epsilon Re = \mathcal{O}(1)$ and the Jacobian $J(a, b) \equiv \partial_y a \partial_z b - \partial_z a \partial_y b$ for fields a and b.

At $\mathcal{O}(\epsilon)$, the χ-component of the fluctuation momentum equation requires

$$J(\psi_1', \overline{u}_0) \quad = \quad 0, \tag{46}$$

a key constraint that will enable significant simplifications in the following analysis. The $\mathcal{O}(\alpha\epsilon)$ y- and z- components of the fluctuation momentum equation can be combined into a single equation for the χ-component of the fluctuation vorticity:

$$\partial_\tau \Omega_1' + \overline{u}_0 \partial_\chi \Omega_1' \quad = \quad -\partial_z \overline{u}_0 \partial_\chi\left(\partial_z \psi_1'\right) - \partial_y \overline{u}_0 \partial_\chi\left(\partial_y \psi_1'\right). \tag{47}$$

Restricting attention to equilibrium lower branch ECS, we seek single χ-mode solutions of the form

$$\psi_1' \quad = \quad F(\overline{u})\cos\chi + G(\overline{u})\sin\chi, \tag{48}$$

$$\Omega_1' \quad = \quad \Omega_c(\overline{u})\cos\chi + \Omega_s(\overline{u})\sin\chi, \tag{49}$$

where the subscript 0 on the leading order mean streamwise velocity component has been omitted here (and will be henceforth) for brevity of notation. The Poisson equation relating the fluctuation streamfunction and vorticity yields

$$\Omega_c \quad = \quad |\nabla_\perp \overline{u}|^2 F'' + \left(\nabla_\perp^2 \overline{u}\right) F', \tag{50}$$

$$\Omega_s \quad = \quad |\nabla_\perp \overline{u}|^2 G'' + \left(\nabla_\perp^2 \overline{u}\right) G', \tag{51}$$

16

where a prime on $F(\overline{u})$ or $G(\overline{u})$ denotes ordinary differentiation. Finally, substituting into equation (47) gives

$$F'' + \left[\frac{\nabla_\perp^2 \overline{u}}{|\nabla_\perp \overline{u}|^2} + \frac{1}{\overline{u}} \right] F' = 0. \tag{52}$$

An analogous relation is easily derived for $G(\overline{u})$. For equation (52) to have a solution, the term in brackets must be a function only of $\overline{u}$:

$$\frac{\nabla_\perp^2 \overline{u}}{|\nabla_\perp \overline{u}|^2} + \frac{1}{\overline{u}} = Q(\overline{u}). \tag{53}$$

Presuming this to be the case,

$$F'(\overline{u}) = a \exp\left[-\int_0^{\overline{u}} Q(\tilde{u}) d\tilde{u} \right] \tag{54}$$

for a to-be-determined constant a.

Inspection of equations (53) and (54) shows that the fluctuation velocity field in the y–z plane, which is proportional to F', is singular at $\bar{u} = 0$, with $F'(\bar{u}) = O(1/\bar{u})$ as $\bar{u} \to 0$. As shown in [6], this critical layer singularity is regularized by viscous forces for the lower branch ECS. Reinstating viscous diffusion in the steady version of equation (47) yields

$$\overline{u}\partial_\chi \Omega_1' = -\partial_z \overline{u}\partial_\chi \left(\partial_z \psi_1' \right) - \partial_y \overline{u}\partial_\chi \left(\partial_y \psi_1' \right) + \frac{1}{\hat{R}}\nabla_\perp^2 \Omega_1'. \tag{55}$$

Upon substituting for ψ_1' and Ω_1' from equations (48) and (49), noting that the slaving relation (46) continues to be asymptotically valid within the critical layer, a pair of coupled, fourth-order ordinary differential equations (ODEs) is obtained for F and G. The ODE for F reads

$$\frac{1}{\hat{R}}\left\{ F'''' + \left(\frac{2\nabla_\perp \overline{u} \cdot \nabla_\perp |\nabla_\perp \overline{u}|^2 + 2|\nabla_\perp \overline{u}|^2 \nabla_\perp^2 \overline{u}}{|\nabla_\perp \overline{u}|^4} \right) F''' \right.$$
$$+ \left(\frac{2\nabla_\perp \overline{u} \cdot \nabla_\perp (\nabla_\perp^2 \overline{u}) + (\nabla_\perp^2 \overline{u})^2 + 2|\nabla_\perp (\nabla_\perp \overline{u})|^2 + 2\nabla_\perp \overline{u} \cdot \nabla_\perp (\nabla_\perp^2 \overline{u})}{|\nabla_\perp \overline{u}|^4} \right) F''$$
$$\left. + \left(\frac{\nabla_\perp^4 \overline{u}}{|\nabla_\perp \overline{u}|^4} \right) F' \right\} - \overline{u}\left(\frac{|\nabla_\perp \overline{u}|^2 G'' + (\nabla_\perp^2 \overline{u})G'}{|\nabla_\perp \overline{u}|^4} \right) - \left(\frac{|\nabla_\perp \overline{u}|^2}{|\nabla_\perp \overline{u}|^4} \right) G' = 0, \tag{56}$$

with a similar equation holding for G. Within the critical layer, gradients with respect to $\overline{u}$ are large, $\mathcal{O}(\hat{R}^{1/3})$, but $\overline{u}$ (as a function of y and z) is smooth, implying $\overline{u} = \mathcal{O}(\hat{R}^{1/3})$. Hence, asymptotically, this ODE simplifies to

$$\frac{1}{\hat{R}}F'''' - \overline{u}\frac{|\nabla_\perp \overline{u}|^2}{|\nabla_\perp \overline{u}|^4}G'' - \frac{|\nabla_\perp \overline{u}|^2}{|\nabla_\perp \overline{u}|^4}G' = 0. \tag{57}$$

For this resulting equation to be well posed, $1/|\nabla_\perp \overline{u}|^2 = (Q(\overline{u}) - 1/\overline{u})/\nabla_\perp^2 \overline{u}$ must be a function solely of $\overline{u}$. In fact, consideration of other steady critical layers arising in shear flows and regularized by viscous diffusion of momentum strongly suggests that the constraint

$$|\nabla_\perp \overline{u}|^2 \equiv (\partial_y \overline{u})^2 + (\partial_z \overline{u})^2 = C \tag{58}$$

17

must be satisfied for some (to-be-determined) constant C. Presuming this to be the case, and employing the rescaling

$$\overline{u} \ \sim \ \hat{R}^{-1/3}U, \tag{59}$$

the linear, non-constant coefficient ODEs for $\mathcal{F}(U) \equiv F(\overline{u})$ and $\mathcal{G}(U) \equiv G(\overline{u})$ become

$$\mathcal{F}'''' - \frac{1}{C}U\mathcal{G}'' - \frac{1}{C}\mathcal{G}' \ = \ 0, \tag{60}$$

$$\mathcal{G}'''' + \frac{1}{C}U\mathcal{F}'' + \frac{1}{C}\mathcal{F}' \ = \ 0. \tag{61}$$

Finally, defining $\mathcal{H} \equiv \mathcal{F} + i\mathcal{G}$ and $\mathcal{J} \equiv \mathcal{H}'$, we obtain

$$\mathcal{J}'' + i\left(\frac{1}{C}\right)U\mathcal{J} \ = \ K \tag{62}$$

for some constant K. Following Hall & Sherwin (see equation (2.22) in [6]), the solution for $\mathcal{J}(U)$ that decays as $|U| \to \infty$ may be expressed in terms of Scorer functions but can be further manipulated to yield

$$\mathcal{J}(U) \ = \ -KC^{2/3}\int_0^\infty \exp\left[i\frac{1}{C^{1/3}}Us - \frac{s^3}{3}\right]ds. \tag{63}$$

As $|U| \to \infty$, the real (imaginary) part of $\mathcal{J}(U)$ matches smoothly with the solution (54) for $F'(\overline{u})$ (the corresponding solution for $G'(\overline{u})$), as $|\overline{u}| \to 0$. This asymptotic matching yields an algebraic relation between the constants K and a. Thus, apart from the constants a and C, v_1' and w_1' are completely determined by this analysis, at least as a function of the unknown $\overline{u}(y,z)$ – a significant simplification.

The Reynolds stress divergence across the critical layer drives a mean flow in the y–z plane; namely, the rolls. The leading-order dominant balance in equation (44) *within* the critical layer requires

$$\frac{1}{R}\nabla_\perp^2\overline{\Omega}_1 \ \sim \ -\left(\partial_z^2 - \partial_y^2\right)\overline{v_1'w_1'} - \partial_z\left[\partial_y\left(\overline{v_1'v_1'} - \overline{w_1'w_1'}\right)\right], \tag{64}$$

where it has been posited that the roll velocity is smooth but that there is a jump in the χ-component of mean vorticity $\overline{\Omega}_1$ across the critical layer, as can be verified *a posteriori*. It proves convenient to consider this equation in $(\overline{u},z)$ rather than Cartesian (y,z) coordinates. Specifically, we write $\overline{\Omega}_1(y,z) = \tilde{\Omega}(\overline{u},z)$ and $\overline{\psi}_1(y,z) = \tilde{\psi}(\overline{u},z)$, and recall $\psi_1'(\chi,y,z) = F(\overline{u})\cos\chi + G(\overline{u})\sin\chi$. After much algebraic manipulation, equation (64) can be expressed as

$$\frac{1}{R}|\nabla_\perp\overline{u}|^2\partial_{\overline{u}}^2\tilde{\Omega} \sim \left[\left(F'(\overline{u})\right)^2 + \left(G'(\overline{u})\right)^2\right]'\left\{\partial_y(\partial_z\overline{u})\left[(\partial_y\overline{u})^2 - (\partial_z\overline{u})^2\right]\right.$$

$$\left. + (\partial_y\overline{u})(\partial_z\overline{u})\left[\partial_z^2\overline{u} - \partial_y^2\overline{u}\right]\right\}. \tag{65}$$

18

Integrating this equation from $\overline{u} = 0$ to $\overline{u} = \Delta$, *i.e.* from the center to the upper edge of the critical layer, yields an effective boundary condition on the "outer" mean vorticity as the critical layer is approached from above:

$$\partial_{\overline{u}}\tilde{\Omega}\Big|_{\overline{u}\to 0^+} \sim \frac{R}{2}\left\{\frac{\partial_y(\partial_z\overline{u})\left[(\partial_y\overline{u})^2 - (\partial_z\overline{u})^2\right] + (\partial_y\overline{u})(\partial_z\overline{u})\left[\partial_z^2\overline{u} - \partial_y^2\overline{u}\right]}{|\nabla_\perp\overline{u}|^2}\right\}_{\overline{u}\to 0^+}$$
$$\times\left\{\left[\left(F'(\Delta)\right)^2 + \left(G'(\Delta)\right)^2\right] - \left[\left(F'(0)\right)^2 + \left(G'(0)\right)^2\right]\right\}. \quad (66)$$

The outer problem for the mean flow in the y–z plane *above* the critical layer (above the white region in figure 12(a) top panel for example) also requires a boundary condition on $\tilde{\psi}$. This condition is obtained by noting that $\tilde{\Omega} \sim |\nabla_\perp\overline{u}|^2\partial_{\overline{u}}^2\tilde{\psi}$ within the critical layer and, hence, that

$$\partial_{\overline{u}}\tilde{\psi}\Big|_{\overline{u}\to 0^+} \quad \sim \quad \frac{1}{|\nabla_\perp\overline{u}|^2}\int_{\overline{u}=0}^{\overline{u}=\Delta}\tilde{\Omega}\,d\overline{u}. \quad (67)$$

Note that both equations (66) and (67) implicitly enforce the symmetry conditions $\partial_{\overline{u}}\tilde{\Omega} = \partial_{\overline{u}}\tilde{\psi} = 0$ along $\overline{u} = 0$ and must satisfy the constraint (58), which applies (asymptotically) everywhere within the critical layer.

We may now summarize the algorithm for computing lower branch ECS, satisfying Wang *et al.* scalings [21], in the small-α limit with $\hat{R} \equiv \alpha Re \gg 1$ and $R = \epsilon Re = \mathcal{O}(1)$. In the limit $Re \to \infty$, the critical layer becomes infinitely thin, and we compute the solution in the non-rectangular y–z domain above the critical layer; by symmetry, we can reconstruct the solution below the critical layer. First, an initial guess for $\overline{u}(y, z)$ in this domain is required; again, it should be emphasized that this initial and all subsequent iterates must satisfy equation (58) along $\overline{u} = 0$, as noted above. We then march

$$\partial_T\tilde{\Omega} + (\partial_y\overline{u})\left(\partial_{\overline{u}}\tilde{\psi}\partial_z\tilde{\Omega} - \partial_z\tilde{\psi}\partial_{\overline{u}}\tilde{\Omega}\right) \quad \sim \quad \frac{1}{R}\left[|\partial_\perp\overline{u}|^2\partial_{\overline{u}}^2\tilde{\Omega} + \left(\nabla_\perp^2\overline{u}\right)\partial_{\overline{u}}\tilde{\Omega} + \partial_z^2\tilde{\Omega}\right], \quad (68)$$
$$|\partial_\perp\overline{u}|^2\partial_{\overline{u}}^2\tilde{\psi} + \left(\nabla_\perp^2\overline{u}\right)\partial_{\overline{u}}\tilde{\psi} + \partial_z^2\tilde{\psi} \quad = \quad \tilde{\Omega} \quad (69)$$

to steady state on a discrete $(\overline{u}, z)$ grid. Note that, asymptotically, the Reynolds stress terms in equation (44) are consistently omitted in equation (68). The mean flow is, instead, driven by the effective boundary conditions just above the critical layer (*i.e.* as $\overline{u} \to 0^+$): equations (66) and (67). Imposition of these boundary conditions requires evaluation of the quadrature (63) for the fluctuation fields within the critical layer. Finally, the solution for $\tilde{\psi}(\overline{u}, z)$ along with the initial iterate for $\overline{u}(y, z)$ can be used to reconstruct $\overline{\psi}_1(y, z)$ in the region above the critical layer. Then equation (43) can be marched to steady state in the discrete y–z domain (subject to $\overline{u} = 0$ at the "old" location of the critical layer), and the entire iteration repeated until convergence.

5 Discussion

In the present investigation, we have derived a model of the dynamics near lower branch ECS in plane Waleffe flow. This model is asymptotically valid in the limit of high Reynolds
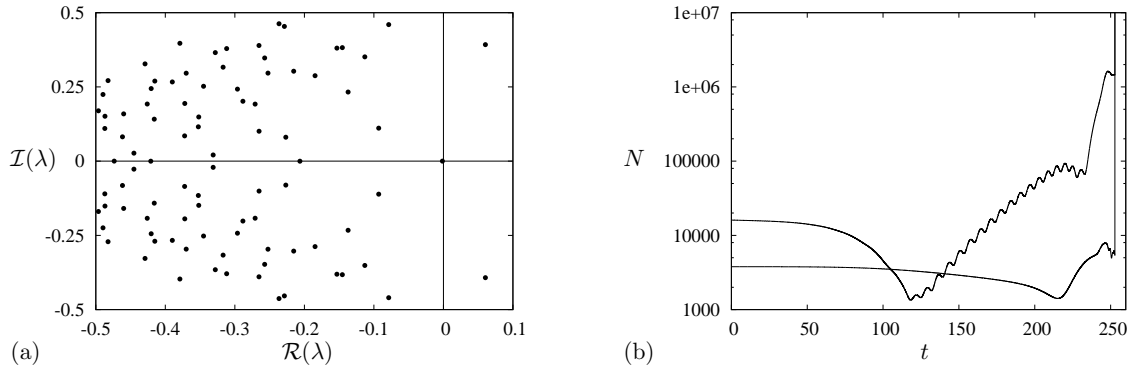
Figure 13: (a) Eigenvalues λ for the iterate shown in figure 12, with $\mathcal{R}(\lambda)$ the growth rate of the fluctuation and $\mathcal{I}(\lambda)$ the temporal pulsation. (b) Time integration of the "complete" reduced system (35)–(39) starting from this state. The solutions are represented by the 2-norm of the Fourier spectrum N for the mean variables (bottom curve) and the fluctuations (oscillating curve).

numbers. We have also developed an algorithm based on this model to obtain good estimates of lower branch solutions given only an initial profile for the streamwise averaged velocity. Using this novel iterative algorithm, we were able to compute the near lower branch flow state shown in figure 12, which, in turn, should provide an excellent first iterate for a standard Newton solver. Other solutions can easily be sought by imposing an appropriate initial condition for the streamwise averaged velocity or by using the small-α approach developed in section 4. The merit of this approach is two-fold: (i) the problem can be solved for asymptotically large Re without the need to resolve the critical layer; and (ii) the fluctuation system has been reduced to a quadrature. With a solution for asymptotically-small α available, solutions for finite α can be computed using standard numerical continuation software.

An alternative method can also be used to obtain lower branch solutions: edge-tracking [16]. Designed to find edge states, this technique involves time-stepping the governing equations for initial conditions with different amplitudes. This methods exploits the fact that some edge solutions are once unstable: if the amplitude is too small, the initial condition will decay to the laminar solution; if the amplitude is too large, the initial condition will grow to reach a different state. By identifying the divergence in the decay/growth behavior, linear combinations of the diverging solutions can be formed to generated initial conditions that, when time-advanced, continue to track the edge for longer and longer durations. The edge can be followed in this way, simply using a time-stepper. The stability of the state we have found is indicated in figure 13(a). It is represented in the complex λ plane, where the real part $\mathcal{R}(\lambda)$ represents the temporal growth rate of the perturbation and the imaginary part $\mathcal{I}(\lambda)$ the temporal pulsation. There is a $\lambda \approx 0$ mode, representing the fluctuations in figure 12. In addition to this mode are modes with complex conjugate λ with positive real part. The presence of these modes indicates that the solution is unstable with respect to time-dependent fluctuations. It is therefore not an attractive edge solution, in the sense it is not strictly once unstable. Nevertheless, edge-tracking can be used to

20

find new solutions. We implemented a third order Runge–Kutta scheme to discretize in time [17] in the reduced system (35)–(39). A typical simulation result is plotted in figure 13(b). This simulation has been initialized using the state shown in figure 12. Initially, the dynamics are slow, owing to the fact the solution is nearly marginal. Then, oscillations, corresponding to the most unstable mode in figure 13(a), start to grow exponentially. Due to the separation in time scales, the mean variables do not respond, enabling the fluctuations to grow. At approximately $t = 200$, the fluctuations become $\mathcal{O}(1/\epsilon)$, violating the lower branch asymptotic scaling and suggesting the dynamics is moving toward upper branch solutions or turbulent states. Indeed, by continuing the computation a little bit further, the code blew up as a result of the undamped growth of the fluctuations, generating intense rolls that violated the CFL condition. This process seems unavoidable as the tests we ran with different time steps resulted in a similar blow up behavior, albeit at slightly different times despite a converged simulation until then. These simulations do however provide useful information: the quasi-linear behavior of the fluctuations and time scale separation imply that fluctuations and mean variables evolve in a rather decoupled manner. Classic edge-tracking is therefore not possible as two different amplitudes are needed (one for the fluctuations and one for the mean variables) instead of one.

To cope with these difficulties, we propose to simulate the following augmented system:

$$\zeta_1 \partial_t \overline{u}^0 + \partial_y \overline{\psi}_1^0 \partial_z \overline{u}^0 - \partial_z \overline{\psi}_1^0 \partial_y \overline{u}^0 = \tfrac{1}{R} \nabla_\perp^2 \overline{u}^0 + \tfrac{\sqrt{2}\pi^2}{4R} \sin(\pi y/2), \tag{70}$$

$$\zeta_1 \partial_t \overline{\omega}_1^0 + J\left(\overline{\psi}_1^0, \overline{\omega}_1^0\right) + 2\left(\partial_y^2 - \partial_z^2\right) \overline{\mathcal{R}(v_1' w_1'^*)} + 2\partial_z \partial_y \left(\overline{w_1' w_1'^*} - \overline{v_1' v_1'^*}\right) = \tfrac{1}{R} \nabla_\perp^2 \overline{\omega}_1^0, \tag{71}$$

$$\partial_t u_1' + i\alpha \overline{u}^0 u_1' + v_1' \partial_y \overline{u}^0 + w_1' \partial_z \overline{u}^0 = -i\alpha p_1' + \tfrac{\epsilon}{R} \nabla_\perp^2 u_1', \tag{72}$$

$$\partial_t v_1' + i\alpha \overline{u}^0 v_1' + \zeta_2 \left(v_1' \partial_y v_1' + w_1' \partial_z v_1'\right) = -\partial_y p_1' + \tfrac{\epsilon}{R} \nabla_\perp^2 v_1', \tag{73}$$

$$\partial_t w_1' + i\alpha \overline{u}^0 w_1' + \zeta_2 \left(v_1' \partial_y w_1' + w_1' \partial_z w_1'\right) = -\partial_z p_1' + \tfrac{\epsilon}{R} \nabla_\perp^2 w_1', \tag{74}$$

$$i\alpha u_1' + \partial_y v_1' + \partial_z w_1' = 0. \tag{75}$$

This system is a replica of equations (27)–(33) in the case of $\mathcal{O}(1)$ varying solutions in the streamwise coordinate with a few modifications. The first one concerns the occurrence of ζ_1 terms in equations (70) and (71) where ζ_1 should be ϵ. By replacing ϵ by an $\mathcal{O}(1)$ value, we eliminate the time scale separation, enabling an effective feedback from the mean variables. The second modification is the addition of the terms involving ζ_2 in equations (73) and (74). Provided $\zeta_2 = \mathcal{O}(1)$, these nonlinear terms for the fluctuations will fix their amplitude. Strictly, these terms arise at higher order and hence ζ_2 should equal ϵ to respect our model derivation. Nevertheless, the idea behind this augmented system is to compute the edge for $\zeta_1 = \mathcal{O}(1)$ and $\zeta_2 = \mathcal{O}(1)$ and then, in a process called homotopy, gradually decrease ζ_1 and ζ_2 to obtain an edge solution for $\zeta_1 = \zeta_2 = \epsilon$. At large Re (small ϵ), this solution is a solution of the system (35)–(39).

Once edge solutions are obtained, their dependence on the streamwise wavenumber α will be investigated. Indeed, the current literature has focused on finite-sized boxes, but practical applications of parallel shear flows may involve very long streamwise scales. Thus, our reduced model may provide an effective way to bridge the gap between current simulations and long domains. Another possibility is to use the model to compute more complex solutions exhibiting streamwise modulation by including $\overline{\psi}_1^\delta$ and $\overline{\omega}_1^\delta$ or to obtain localized solutions in the spanwise direction by computing in a larger domain. These lines of
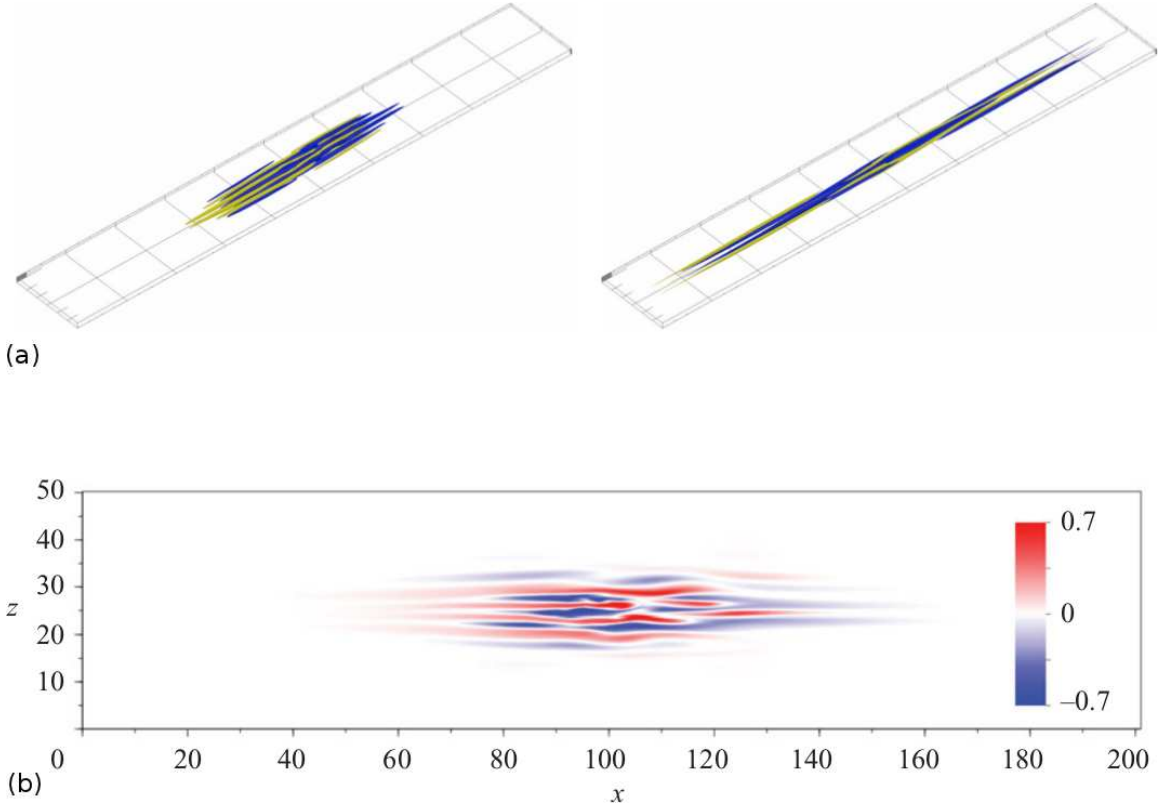
(a)

(b)

Figure 14: (a) Instantaneous snapshots of the edge state for $Re = 375$ (left) and $Re = 1000$ (right). Three-dimensional isocontours of the streamwise velocity perturbation are shown. Only part of the spanwise domain is shown here. After Duguet *et al.* [1]. (b) Localized turbulence seed at $Re = 400$ represented via the streamwise velocity in the $y = 0$ plane. After Schneider *et al.* [15].

inquiry are motivated by the edge solutions obtained by Duguet *et al.* [1] and Schneider *et al.* [15] and shown in figure 14. Computing these solutions using the reduced model would shed light on the structure of the edge at high Reynolds numbers and on various types of localization in parallel shear flows. Finally, it should be noted that although Waleffe flow has been used here as a simpler surrogate for Couette flow, there have been no systematic comparative studies of these flows. Such a comparison would inform future studies and provide impotant context for the current investigation.

Acknowledgments

22

for their unconditional support.

References

[1] Y. DUGUET, P. SCHLATTER, AND D. S. HENNINGSON, *Localized edge states in plane Couette flow*, Phys. Fluids, 21 (2009), p. 111701.

[2] M. FRIGO AND S. G. JOHNSON, *The Design and Implementation of FFTW3*, Proceedings of the IEEE, 93 (2005), pp. 216–231. Special issue on "Program Generation, Optimization, and Platform Adaptation".

[3] J. F. GIBSON, *Channelflow: A spectral Navier-Stokes simulator in C++*, tech. rep., U. New Hampshire, 2012. `Channelflow.org`.

[4] J. F. GIBSON, J. HALCROW, AND P. CVITANOVIĆ, *Equilibrium and travelling-wave solutions of plane Couette flow*, J. Fluid Mech., 638 (2009), pp. 243–266.

[5] I. GROOMS, K. JULIEN, AND B. FOX-KEMPER, *On the interactions between planetary geostrophy and mesoscale eddies*, Dynam. Atmos. Ocean, 51 (2011), pp. 109–136.

[6] P. HALL AND S. J. SHERWIN, *Streamwise vortices in shear flows: Harbingers of transition and the skeleton of coherent structures*, J. Fluid Mech., 661 (2010), pp. 178–205.

[7] G. KAWAHARA AND S. KIDA, *Periodic motion embedded in plane Couette turbulence: Regeneration cycle and burst*, J. Fluid Mech., 449 (2001), pp. 291–300.

[8] R. KLEIN, *Scale-dependent models for atmospheric flows*, Annu. Rev. Fluid Mech., 42 (2010), pp. 249–274.

[9] R. B. LEHOUCQ, D. C. SORENSEN, AND C. YANG, *ARPACK Users Guide: Solution of Large Scale Eigenvalue Problems by Implicitly Restarted Arnoldi Methods.*, 1997.

[10] A. J. MAJDA AND R. KLEIN, *Systematic multiscale models for the Tropics*, J. Atmos. Sci., 60 (2003), pp. 393–408.

[11] P. MANNEVILLE, *Spots and turbulent domains in a model of transitional plane Couette flow*, Theoret. Comput. Fluid Dynamics, 18 (2004), pp. 169–181.

[12] M. NAGATA, *Three-dimensional finite-amplitude solutions in plane Couette flow: Bifurcation from infinity*, J. Fluid Mech., 217 (1990), pp. 519–527.

[13] P. J. SCHMID AND D. S. HENNINGSON, *Stability and Transition in Shear Flows*, no. 142 in Applied Mathematical Sciences, Springer, 2001.

[14] T. M. SCHNEIDER, J. F. GIBSON, M. LAGHA, F. D. LILLO, AND B. ECKHARDT, *Laminar-turbulent boundary in plane Couette flow*, Phys. Rev. E, 78 (2008), p. 037301.

[15] T. M. SCHNEIDER, D. MARINC, AND B. ECKHARDT, *Localized edge states nucleate turbulence in extended plane Couette cells*, J. Fluid Mech., 646 (2010), pp. 441–451.

[16] J. D. Skufca, J. A. Yorke, and B. Eckhardt, *Edge of chaos in parallel shear flow*, Phys. Rev. Lett., 96 (2006), p. 174101.

[17] P. R. Spalart, R. D. Moser, and M. M. Rogers, *Spectral methods for the Navier–Stokes equations with one infinite and two periodic boundary conditions*, J. Comp. Phys., 96 (1991), pp. 297–324.

[18] C. G. Speziale, *Analytical methods for the development of Reynolds-stress closures in turbulence*, Annu. Rev. Fluid Mech., 23 (1991), pp. 107–157.

[19] D. Viswanath, *Recurrent motions within plane Couette turbulence*, J. Fluid Mech., 580 (2007), pp. 339–358.

[20] F. Waleffe, *On a self-sustaining process in shear flows*, Phys. Fluids, 9 (1997), pp. 883–900.

[21] J. Wang, J. Gibson, and F. Waleffe, *Lower branch coherent states in shear flows: Transition and control*, Phys. Rev. Lett., 98 (2007), p. 204501.